Adaptive High-Order Sliding-Mode Low-speed Control With RBF Neural Network Nonlinear Disturbance Observer for PMSM Drive System

Weichao Wang, Yongqiang Ye, *Senior Member, IEEE*, Xudong Chen, and Yongchao Yuan

***Abstract*—The impact of friction torque, cogging torque, and uncertain disturbances on permanent magnet synchronous motor drive system (PMSMDS) is more pronounced at low speeds compared to high speeds. Therefore, this article proposes an adaptive integral high-order sliding-mode low-speed composite controller (AIHOSMC) based on an radial basis function neural network (RBFNN) nonlinear disturbance observer (RBFNNDO), aimed at enhancing speed tracking accuracy and antidisturbance capability. First, a PMSMDS model that includes adverse disturbances is established, and the fast-changing and slow-changing characteristics of these disturbances are analyzed. Then, AIHOSMC is developed to enhance dynamic response speeds, eliminate steady-state errors, and dynamically adjust control gains to achieve finite-time convergence (FTC) of PMSMDS. In addition, by combining the nonlinear disturbance observer (NDO) with the infinite approximation capability of RBF neural networks, an RBFNNDO is utilized to accurately estimate fast-changing and slow-changing disturbances in real time, improving the control performance of the AIHOSMC. Thereafter, a closed-loop stability analysis of the proposed controller is performed using Lyapunov theorem. Finally, experimental results validate the effectiveness of the proposed controller, demonstrating significant improvements in low-speed tracking accuracy and antidisturbance performance in PMSMDS.**

***Index Terms*—Adaptive high-order sliding-mode control, low-speed control, nonlinear disturbance observer (NDO), permanent magnet synchronous motor drive system (PMSMDS), RBF neural network approximation.**

I. INTRODUCTION

PERMANENT magnet synchronous motor drive system (PMSMDS) is widely utilized in power transmission systems, such as industrial uncrewed aerial vehicles [1], automated guided vehicles [2], and new energy generation systems [3], due to its high efficiency, high integration, wide speed regulation range, and reliability. As application fields expand, modern industry demands higher tracking accuracy, faster dynamic response, and better antidisturbance capabilities from PMSMDS. Notably, in systems [1], [2], [3], PMSMDS operates at low speeds where the effects of cogging and friction torque are more pronounced compared to those at high speeds [4], [5], [6]. Both cogging torque and friction torque are nonlinear functions related to position and speed, respectively. The time-varying operating conditions result in complex disturbance mechanisms that seriously affect the dynamic and static characteristics of the system [7], [8]. Attributing adverse disturbances and uncertainty to lumped disturbance is a mainstream method, but it has its limitations [9], [10]. Analyzing the mechanism of disturbance and compensating for it purposefully is the key to improving the control performance of low-speed PMSMDS.

Extended state observer (ESO) and nonlinear disturbance observer (NDO) are important methods for observing and compensating disturbances. However, ESO typically requires systems to be represented in a companion form [11], and high gain peaks and parameter sensitivity need to be considered during the design process [12], [13]. NDO has an independent and relatively simple control structure, with good dynamic performance and global stability [14]. The ability of NDO to handle nonlinear disturbances is superior to ESO, but it is generally used for slow-changing disturbances [14], [15]. The parallel observer can achieve online adaptive identification of friction torque [7], but its adaptive approximation ability is limited and insufficient for handling nonlinearities. To effectively handle nonlinear and fast-changing disturbances at low speeds, a radial basis function neural network (RBFNN) based on online adaptive optimization is a feasible strategy. Unlike data-driven RBFNN, it does not require complex training rules and only relies on the input state of the system [16], [17]. It can effectively solve uncertainties, input nonlinearities, and external disturbances that NDO cannot completely solve, and demonstrates good approximation ability to

Received 19 October 2024; revised 12 January 2025 and 8 March 2025; accepted 1 April 2025. Date of publication 11 April 2025; date of current version 26 May 2025. This work was supported by the 2024 Independent Project on Autonomous Control Technology for Aircraft in the Engineering Research Center of the Ministry of Education, the People's Republic of China. Recommended for publication by Associate Editor R. Kennel. *(Corresponding author: Yongqiang Ye.)*

Weichao Wang, Yongqiang Ye, and Xudong Chen are with the College of Automation Engineering, Nanjing University of Aeronautics and Astronautics, Nanjing 211106, China (e-mail: weichao0704@nuaa.edu.cn; melvinye@nuaa.edu.cn; sx2303135@nuaa.edu.cn).

Yongchao Yuan is with the China Academy of Machinery Science and Technology Qingdao Branch Company LTD., Qingdao 266300, China (e-mail: yuanyc@camqd.com.cn).

Color versions of one or more figures in this article are available at https://doi.org/10.1109/TPEL.2025.3559890.

Digital Object Identifier 10.1109/TPEL.2025.3559890

fast-changing nonlinear disturbances. Research in [18] and [19] primarily emphasizes the infinite approximation capability of RBFNN for nonlinear problems, focusing on theoretical and simulation aspects without practical verification under complex conditions. Research in [20] and [21] employ RBFNN controllers to tackle the nonlinear and uncertain challenges of induction motor position control systems, achieving promising results, however, further investigation is needed to assess their suitability at low speeds. Practical applications indicate that the multilayer structure of RBFNN can effectively approximate any nonlinear function [22], [23], offering a viable solution for low-speed control of PMSMDS.

In addition to the requirements for antidisturbance capability and robustness, the system state convergence performance, control accuracy, and adaptability to complex operating conditions of PMSMDS are worth further discussion. For instance, the novel parameter estimation method can effectively compensate for the disturbance torque. Nevertheless, triple-step controllers based on PID have limitations in dynamic response [9]. Although numerous studies have proposed relatively intelligent controllers to address these challenges, issues remain. Fuzzy strategies [24], particle swarm optimization methods [25], and quantum genetic algorithms [26] can intelligently optimize the system, but their controller complexity, high model dependency, and difficulty in parameter tuning cannot be ignored. In addition, while focusing on the compensation effects of the observers, further research is needed on the response and convergence speed of the controllers, as well as their adaptability to complex operating conditions.

Compared to the limitations of PID and the complexity of intelligent algorithms, various traditional and enhanced sliding-mode control (SMC) methods [27], [28], [29], [30], [31], [32] have gained popularity due to their unique advantages, such as fast dynamic response, independence from model accuracy, and strong robustness. In [27], improvements to traditional SMC are proposed in both the controller structure and convergence laws to reduce system chattering and accelerate convergence speed. However, the effectiveness of compensating for load disturbances and system uncertainties, treated as total disturbances, remains limited. The super-twisting algorithm in high-order SMC can achieve chattering-free control for systems with relative orders of one. Nonetheless, fixed control gains may lead to parameter overestimation and challenges in achieving finite-time convergence (FTC) [28], [29]. By utilizing dynamic adaptive control gains, it is possible to establish a true high-order sliding mode within a finite time while maintaining strong robustness. The introduction of adaptive control gains undoubtedly enhances robustness of the system [30], [31], however, complex judgment conditions can slow the convergence rate, and an excess of control parameters can complicate optimization, making experimental verification difficult [32]. Inspired by the advantages of high-order sliding-mode and adaptive control theory, this article aims to employ these concepts as the primary controller to achieve precise speed tracking.

This article designs an adaptive integral high-order sliding-mode low-speed composite controller (AIHOSMC) based on RBFNN nonlinear disturbance observer (RBFNNDO) to improve the low-speed control performance of PMSMDS with as low controller complexity as possible. The main contributions are summarized as follows.

1) Unlike [5], [7], [14], [24], this article investigates the performance of PMSMDS under specific low-speed operating conditions where nonlinear characteristics are significantly prominent, a low-speed PMSMDS model is developed, incorporating various adverse disturbances.
2) Unlike [4], [6], [8], [9], [10], [25], [26], a novel RBFNNDO is designed to compensate for disturbance purposefully, which utilizes NDO to estimate slow-changing disturbances and adaptively compensates for fast-changing nonlinear disturbances using the infinite approximation ability of RBFNN, ensuring the low-speed robustness. This is an improvement on the existing research on unified classification and compensation of disturbance.
3) Unlike the adaptive SMC methods proposed in [27], [28], [29], [30], and [31], this article does not provide overall adaptation for the controller, but rather adapts the gains that affect the convergence speed and steady-state error of AIHOSMC to ensure accurate convergence of the system state and adaptability to complex operating conditions, achieving FTC and optimized tracking accuracy of PMSMDS.
4) A unified Lyapunov function, encompassing the main controller, disturbance observer, and adaptive laws, is established to measure the asymptotic stability of the system. Finally, the practicality of the proposed composite controller is validated through experiments conducted on a PMSMDS experimental platform.

II. Low-Speed PMSMDS Modeling

This article uses rotor flux oriented axial and radial magnetic field decoupling strategy, and based on the dq-axis two-phase rotating coordinate frame, a dynamic model of stator voltage and mechanical motion for low-speed PMSMDS can be obtained as

$$\begin{cases} \dot{i}_d = (u_d - R_s i_d - n_p \omega L_q i_q)/L_d \\ \dot{i}_q = (u_q - R_s i_q - n_p \omega L_d i_d - n_p \omega \phi_f)/L_q \\ \ddot{\theta} = (T_e - T_L - T_f - T_{\text{cog}})/J \\ T_e = 1.5 n_p i_q \left[\phi_f + (L_d - L_q)\, i_d\right] \end{cases} \tag{1}$$

where i_d, i_q, u_d, u_q, L_d, and L_q are the stator d-axis and q-axis currents, voltages, inductances, respectively; R_s is the stator resistance; J is the moment of inertia; θ is the rotor position angle; ω is the mechanical actual angular velocity; n_p is the number of pole pairs; ϕ_f is the rotor permanent magnet flux linkage; T_L, T_f, and T_{cog} are the load torque, friction torque, and cogging torque, respectively.

Since the Stirbeck static model T_{fs} cannot describe the time-varying dynamic friction torque characteristics, the friction torque T_f in (1) is described using the LuGre dynamic model, and it can be expressed as [6]

$$\begin{cases} T_{fl}\,(\omega) = b_0 \omega + a_0 \Theta + a_1 \frac{d\Theta}{dt} \\ \frac{d\Theta}{dt} = \omega - b_0 \frac{|\omega|}{Z(\omega)} \\ Z\,(\omega) = \left[T_c + (T_s - T_c) e^{-(\omega/\omega_s)^{\varsigma}}\right] \text{sgn}(\omega) \end{cases} \tag{2}$$

where Θ is the bristle deformation state; a_0 and a_1 are the stiffness and damping coefficients of the bristle, respectively; $Z(\omega)$ is a nonlinear function greater than zero; $a_0\Theta$ is the friction torque caused by the bristle state and is the dominant term in T_{fl}; $a_1(d\Theta/dt)$ and $b_0\omega$ representing Stribeck effect friction torque and viscous friction torque, respectively; b_0 is the coefficient of viscous friction; T_c is the coulomb friction torque, which is related to the pressure on the surface of the object; T_s is the maximum static friction torque; ω_s and ς are empirical parameters, in general, $\omega_s \in [10^{-5}, 10^{-1}]$, $\varsigma = 2$.

The cogging torque is a periodic function related to position, and it is described by Fourier expansion as [9]

$$T_{\text{cog}}(\theta) = \sum_{i=1}^{N_i} A_i \sin\left(n_i \text{LCM}\left(Q_p, 2n_p\right)\theta + \psi_i\right) \tag{3}$$

where A_i is the amplitude of n_ith cogging torque harmonic component; LCM$(Q_p, 2n_p)$ is the least common multiple of the slots number Q_p and the number of poles $2n_p$, in this article, Q_p=12 and $2n_p$=8; ψ_i is the harmonic phase.

Remark 1: $T_{fl}(\omega)$ is a nonlinear function related to ω, which includes Θ and $d\Theta/dt$. When the speed of PMSMDS exceeds zero, $T_{fl}(\omega)$ changes direction instantaneously. Therefore, the operating conditions determine the fast-changing and slow-changing characteristics of $T_{fl}(\omega)$, while the direction change and speed determine the rate of change of the internal state. In addition, the longer PMSMDS runs, the higher the temperature, resulting in reduced friction torque. $T_{\text{cog}}(\theta)$ exhibits central symmetry relative to the stator slots, showing both positive and negative values and demonstrating periodic changes. Although PMSMDS operates at low speed, fast-changing, and slow-changing disturbance torque pulsations occur due to the increase in high-frequency signals as n_i increases.

Based on (1)–(3), taking $e_1 = \theta_{\text{ref}} - \theta$ and $e_2 = \omega_{\text{ref}} - \omega$ as state variables x_1 and x_2, where θ_{ref} and ω_{ref} are the reference position and reference speed, respectively, meanwhile, taking i_q as control variable u, PMSMDS dynamic model in the state-space form can be obtained as

$$\begin{cases} \dot{x} = Ax + B_u u - B_0\left(k_t \Upsilon + \varpi\right) \\ y = Cx \end{cases} \tag{4}$$

where $x = [x_1 \quad x_2]^{\text{T}} = [e_1 \quad e_2]^{\text{T}}$, $A = \begin{bmatrix} 0 & 1 \\ 0 & -k_b \end{bmatrix}$, $B_u = [0 \quad k_u]^{\text{T}}$, $B_0 = C^{\text{T}} = [0 \quad 1]^{\text{T}}$, $k_u = \frac{3n_p\phi_f}{2J}$, $k_b = \frac{b_0}{J}$, $k_t = \frac{1}{J}$, $\varpi = k_b\dot{\theta}_{\text{ref}} + \dot{\omega}_{\text{ref}}$, $\Upsilon = D(x) + F(x)$ is total disturbance that includes fast-changing and slow-changing disturbances, $D = T_L + \rho_1 T_{fl}(\omega) + \rho_2 T_{\text{cog}}(\theta)$ is slow-changing disturbance mainly caused by T_L, where, $0 < \rho_1 < 1$ and $0 < \rho_2 < 1$ are the slow-changing proportional coefficients of $T_{fl}(\omega)$ and $T_{\text{cog}}(\theta)$. $F(x) = f + d + \Delta d$ is fast-changing disturbance, which includes the fast-changing parts of $T_{fl}(\omega)$ and $T_{\text{cog}}(\theta)$ (f), unmodeled disturbance (d), and unknown disturbance on the loading side (Δd), f and d can be written as

$$\begin{cases} f = (1-\rho_1)T_{fl}(\omega) + (1-\rho_2)T_{\text{cog}}(\theta) \\ d = \Delta k_u i_q + \Delta k_b \dot{\theta} + \Delta k_t\left(T_L + T_{fl}(\omega) + T_{\text{cog}}(\theta)\right) \end{cases} \tag{5}$$

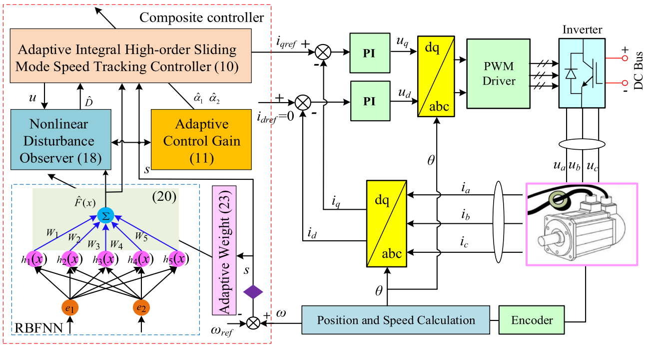

Fig. 1. Control structure of PMSMDS with the proposed controller.

where $\Delta k_u = \frac{3n_p\Delta\phi_f}{2\Delta J}$, $\Delta k_b = -\frac{\Delta b_0}{\Delta J}$, $\Delta k_t = -\frac{1}{\Delta J}$. ΔJ, $\Delta\phi_f$, and Δb_0 are time-varying parameter disturbances during PMSMDS operation.

III. CONTROLLER DESIGN

The goal of this article is to improve the low-speed tracking accuracy and antidisturbance capability of PMSMDS under time-varying conditions, adverse disturbances, and parameter fluctuations. AIHOMSC based on FTC theorem is designed to improve the chattering and limitations of fixed gain in high-order SMC. RBFNNDO aims to improve the estimation accuracy of disturbance. The following presents the design of AIHOSMC, RBFNNDO, and stability analysis, respectively.

Fig. 1 shows the control structure of PMSMDS with the proposed controller. The outer speed loop is based on the composite controller. Both d-axis and q-axis inner current loops are based on PI.

A. Adaptive Integral High-Order Sliding-Mode Controller

To reduce system chattering caused by variable derivatives, an integral is added to the traditional SMC. The integral sliding-mode surface is designed as

$$s = Gx \tag{6}$$

where $G = [g \quad 1]$, $g > 0$, g+p satisfies Hurwitz, and p is a Laplace operator. Constructing the relationship between state variables and control variables, the SMC convergence law is designed as

$$\dot{s} = G\dot{x} = -\beta\text{sgn}(s) - \gamma s \tag{7}$$

where $\beta > 0$ and $\gamma > 0$ are adjustable control parameters. Combining (6), (7) with PMSMDS model (4), the speed tracking control input is designed as

$$i_q^* = \left(GB_u\right)^{-1}\left(-GAx + k_t\Upsilon + \varpi - \beta\text{sgn}(s) - \gamma s\right). \tag{8}$$

Remark 2: If the control parameters are appropriate, (8) can effectively improve the dynamic response of the system. However, chattering is the main drawback of (8) in applications, as the switching term $\beta\text{sgn}(s)$ in the exponential convergence law acts directly on the controller, causing discontinuity in i_q^* and resulting in chattering.

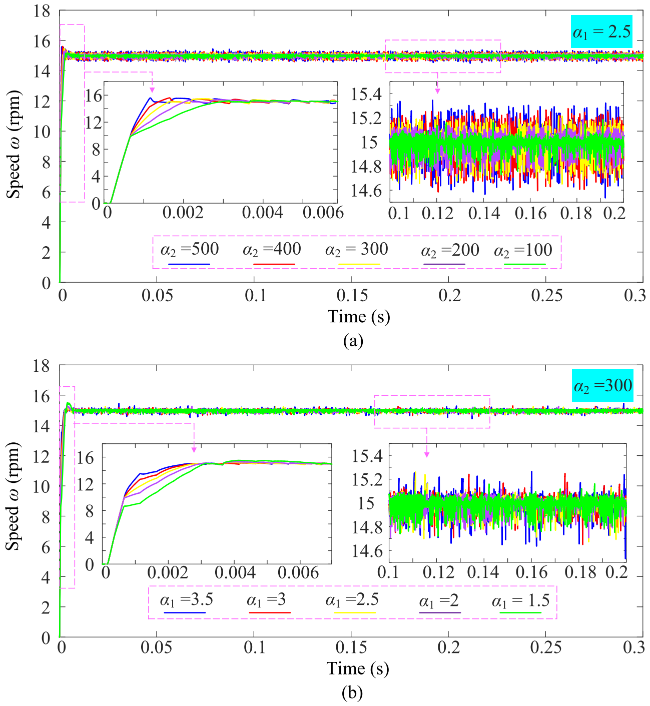

(a)

(b)

Fig. 2. Impact of fixed gain on tracking error and convergence rate. (a) α_1 fixed and α_2 variable. (b) α_2 fixed and α_1 variable.

For controller (8), a high-order super-twisting algorithm is used to reconstruct it as [28]

$$u = (GB_u)^{-1}\begin{pmatrix} -GAx + k_t\Upsilon + \varpi \\ -\alpha_1|s|^{1/2}\mathrm{sgn}(s) - \alpha_2\int \mathrm{sgn}(s) \end{pmatrix} \tag{9}$$

where $\alpha_1 > 0$ and $\alpha_2 > 0$ are adjustable control parameters.

Remark 3: It can be seen from Fig. 2(a) that when α_1 is fixed, as α_2 increases, the convergence speed of the system becomes faster, but the tracking error also increases. From Fig. 2(b), it can be seen that when α_2 is fixed, as α_1 increases, the convergence speed of the system becomes faster, and the tracking error change is not obvious. Tracking error is less sensitive to α_1 than to α_2, but convergence speed is more sensitive to both α_1 and α_2. Unlike β and γ, α_1 and α_2 each have an impact on convergence speed and tracking error. Selecting α_1 and α_2 requires a balance between convergence time and system chattering, making it difficult to establish a true high-order super-twisting controller within a finite time using fixed control gain parameters.

Based on (9), a high-order super-twisting controller with adaptive control gains is designed as

$$u = (GB_u)^{-1}\begin{pmatrix} -GAx + k_t\left(\hat{D} + \hat{F}(x)\right) + \varpi \\ -\hat{\alpha}_1|s|^{1/2}\mathrm{sgn}(s) - \hat{\alpha}_2\int \mathrm{sgn}(s) \end{pmatrix} \tag{10}$$

$$\begin{cases} \dot{\hat{\alpha}}_1 = \begin{cases} w_1\sqrt{\frac{\delta_1}{2}}\mathrm{sgn}(s), & |s| > \ell \\ 0 & |s| \leq \ell \end{cases} \\ \dot{\hat{\alpha}}_2 = 2\varepsilon\dot{\hat{\alpha}}_1, \end{cases} \tag{11}$$

where w_1, δ_1, and ε are both positive parameters, and ℓ is an arbitrary small positive coefficient. Large w_1, δ_1, and ε can obtain smaller tracking error and larger convergence rate.

When the amount of disturbances of PMSMDS is considered, based on (4) and (10), the following can be obtained:

$$\dot{s} = -\hat{\alpha}_1|s|^{1/2}\mathrm{sgn}(s) - \hat{\alpha}_2\int \mathrm{sgn}(s) - k_t\left(\tilde{D} + \tilde{F}(x)\right). \tag{12}$$

Assumption 1: It is reasonable that the adaptive control gains $\hat{\alpha}_1$ and $\hat{\alpha}_2$ are bounded under (11), i.e., there exist positive constants α_1^* and α_2^* such that $\tilde{\alpha}_1 = \alpha_1^* - \hat{\alpha}_1 > 0$ and $\tilde{\alpha}_2 = \alpha_2^* - \hat{\alpha}_2 > 0$, $\forall t \geq 0$.

To effectively analyze the global stability through Lyapunov theorem, it is usually considered to use a convenient form to describe (12) [32]. The following new state variables are introduced:

$$\Phi = \begin{bmatrix} \Phi_1 & \Phi_2 \end{bmatrix}^{\mathrm{T}} = \begin{bmatrix} |s|^{1/2}\mathrm{sgn}(s) & -\hat{\alpha}_2\int \mathrm{sgn}(s) \end{bmatrix}^{\mathrm{T}}. \tag{13}$$

The derivative of Φ is given by

$$\dot{\Phi} = (\Psi_1\Phi - \Psi_2)/(2|\Phi_1|) \tag{14}$$

where $\Psi_1 = \begin{bmatrix} -\hat{\alpha}_1 & 1 \\ -2\hat{\alpha}_2 & 0 \end{bmatrix}$, $\Psi_2 = \begin{bmatrix} k_t(\tilde{D} + \tilde{F}(x)) \\ 0 \end{bmatrix}$.

Remark 4: For $V_0 = \Phi^{\mathrm{T}}\Gamma_1\Phi$, there exists a positive definite matrix $\Gamma_1 = \begin{bmatrix} 4\varepsilon^2 + \sigma & -2\varepsilon \\ -2\varepsilon & 1 \end{bmatrix}$ that satisfies $V_0 \geq 0$, where, σ is an arbitrary small positive coefficient.

The derivative of V_0 is given by

$$\begin{aligned} \dot{V}_0 &= \dot{\Phi}^{\mathrm{T}}\Gamma_1\Phi + \Phi^{\mathrm{T}}\Gamma_1\dot{\Phi} \\ &= -\frac{1}{2|\Phi_1|}\Phi^{\mathrm{T}}\Gamma_2\Phi - \frac{1}{|\Phi_1|}\Phi^{\mathrm{T}}\Gamma_1\Psi_2 \end{aligned} \tag{15}$$

where $\Gamma_2 = -(\Psi_1^{\mathrm{T}}\Gamma_1 + \Gamma_1\Psi_1)$. The following inequality holds:

$$\begin{cases} \lambda_{\min}(*)\|\Phi\|^2 \leq \Phi^{\mathrm{T}} * \Phi \leq \lambda_{\max}(*)\|\Phi\|^2 \\ \|\Phi\| = \sqrt{\Phi_1^2 + \Phi_2^2} \leq |\Phi_1| \end{cases} \tag{16}$$

where $\lambda_{\max}(*)$ and $\lambda_{\min}(*)$ are maximum and minimum eigenvalue of matrix $*$, respectively. Substituting (16) into (15), one can obtain

$$\begin{aligned} \dot{V}_0 \leq &-\frac{\lambda_{\min}(\Gamma_2)}{2\lambda_{\max}^{1/2}(\Gamma_1)}\left(\Phi^{\mathrm{T}}\Gamma_1\Phi\right)^{1/2} \\ &-\lambda_{\min}(\Gamma_1)k_t\left(\left|\tilde{D}\right| - \left|\tilde{F}(x)\right|\right). \end{aligned} \tag{17}$$

Remark 5: It can be observed that if $\Phi \to 0$ in finite time then $s \to 0$ and $\dot{s} \to 0$ in finite time. The transformation in (13)–(17) will be included in the global Lyapunov function stability analysis of PMSMDS. The complete proof is in Section III-C.

B. RBF Neural Network Nonlinear Disturbance Observer

In practical PMSMDS (4), Υ is unavoidable and undetectable. Typically, NDO utilizes internal state variables to observe unknown disturbances, thereby enhancing system robustness. Given the limitations of NDO in accurately observing fast-changing disturbances and parameter uncertainties, the infinite approximation capability of RBFNN is utilized to more effectively estimate disturbances.

To estimate slow-changing disturbances, NDO can be designed as

$$\begin{cases} \dot{\chi} = -\eta_1 k_t \chi - \eta_1 \left(k_t \eta_1 \omega + k_u i_q - k_t F(x) - k_b \omega \right) \\ \hat{D} = -\chi - \eta_1 \omega \end{cases} \tag{18}$$

where χ is the internal state of NDO, and $\eta_1 > 0$ is the observer gain. Define the observer error as $\tilde{D} = D - \hat{D}$, and taking the derivative of $\tilde{D}$ and substituting (18) into it yields

$$\begin{aligned} \dot{\tilde{D}} &= \dot{D} - \dot{\hat{D}} \\ &= \dot{D} + \dot{\chi} + \eta_1 \dot{\omega} \\ &= \dot{D} - \eta_1 k_t \left(-\hat{D} - \eta_1 \omega \right) - \eta_1^2 k_t \omega \\ &\quad + \eta_1 k_t F(x) + \eta_1 k_b \omega - \eta_1 k_u i_q \\ &\quad + \eta_1 k_u i_q - \eta_1 k_b \omega - \eta_1 k_t D - \eta_1 k_t F(x) \\ &= \dot{D} - \eta_1 k_t \tilde{D}. \end{aligned} \tag{19}$$

Assumption 2: The slow-changing disturbance D is bounded and it changes slowly with time, i.e., $|D| \leq \bar{D}$ and $\dot{D} \approx 0$, where $\bar{D}$ is an unknown positive constant.

Inspired by [18], [19], [20], [21], $F(X)$ is defined over a compact set U, which can be described by an RBFNN system $F(X) = W^{\mathrm{T}} h(X)$ where $W = [W_1, \ldots, W_m]^{\mathrm{T}}$ is the weights vector, $X = [X_1, \ldots, X_n]^{\mathrm{T}} \in \mathbb{R}^n$ is the input variable of the RBFNN system, $h(X) = [h_1, \ldots, h_n]^{\mathrm{T}}$ stands for the RBFNN hidden layer output vector, which is described as

$$h_j(X) = \frac{1}{\sqrt{2\pi} b_j} \exp\left(-\frac{\left\| X - c_j \right\|^2}{2 b_j^2} \right) \tag{20}$$

where c_j is the coordinate vector of the center point of the Gaussian basis function of the jth neuron variable in the hidden layer, $b = [b_1, \ldots, b_m]^{\mathrm{T}}$, b_j is the width of the Gaussian basis function of the jth neuron variable in the hidden layer, $i = 1, 2, \ldots, n$, $j = 1, 2, \ldots, m$.

Remark 6: RBFNN transforms the input vector from the input layer to the hidden layer, which is equivalent to mapping a large amount of data from low-dimensional space to high-dimensional space. The RBFNN based on data-driven utilizes the learning ability of NN to achieve optimization goals. The training process is highly dependent on the training data, requiring additional experiments and time-consuming training processes [22]. In contrast, the RBFNN based on online optimization can reduce dependence on training data and adapt well to changes in operating conditions [16], [23]. In general, the approximation efficiency of neural networks increases with the increase of the number of hidden nodes, but the selection of the number of hidden nodes is limited by the computing power of the processor. In real-time systems running at millisecond speeds, the usual practice is to select approximately 5–20 neurons based on previous experience [21].

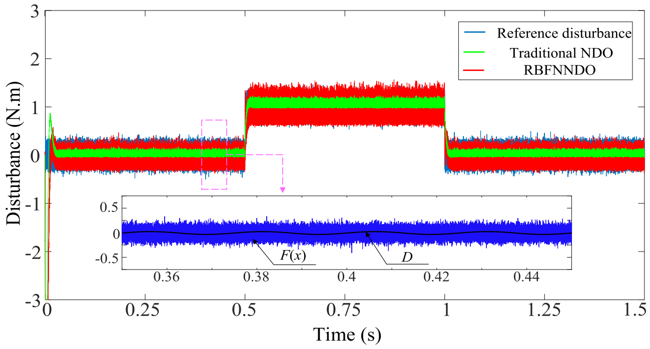

Fig. 3. Comparison of observation effects of different observers.

This article adopts a 2-5-1 RBFNN structure, i.e., $m = 5, n = 2$. The output of RBFNN can be approximated as $F(x) = \hat{W}^{\mathrm{T}} h(x)$, and there is an ideal weight value $W^* = [W_1^*, \ldots, W_m^*]^{\mathrm{T}}$, which can be obtained by

$$W^* = \arg \min_{W \in \mathbb{R}^n} \left[\sup_{x \in U} \left| \hat{W}^{\mathrm{T}} h(x) - W^{\mathrm{T}} h(x) \right| \right] \tag{21}$$

where $\hat{W}$ is the estimated value of W^* and W^* is bounded, i.e., $\|W^*\| \leq \mu_{\max}$, $\mu_{\max}$ is a constant. Therefore, $F(x)$ can be rewritten as

$$F(x) = W^{*\mathrm{T}} h(x) + \varepsilon_W \tag{22}$$

where ε_W is the minimum approximation error and bounded, i.e., $\|\varepsilon_W\| \leq \varepsilon_{W\max}$, $\varepsilon_{W\max}$ is a constant.

In order to quickly approximate the optimal weights of the neural network, and to make the observation error and system tracking error approach zero at the same time, a novel adaptive law of the weights is designed as

$$\dot{\hat{W}} = -\eta_2 \left(|\Phi_1|^{1/2} \operatorname{sgn}(\Phi_1) h(x) + \tau \hat{W} \right) \tag{23}$$

where $\eta_2 > 0$ and $\tau > 0$ are adjustable control parameters. Define $\tilde{W} = W^* - \hat{W}$, and the estimated error is given by

$$\tilde{F}(x) = F(x) - \hat{F}(x) = \tilde{W}^{\mathrm{T}} h(x) + \varepsilon_W. \tag{24}$$

Fig. 3 shows the observation effects of traditional NDO and RBFNNDO, where the reference consists of fast-changing and slow-changing disturbance. It can be clearly seen that traditional NDO only has a good observation effect on slow-changing disturbance, but cannot observe the fast-changing disturbance, resulting in a large observation error and limiting the compensation effect. However, RBFNNDO has made good observations on both fast-changing and slow-changing disturbance, with an observation error close to zero, thus compensating for the shortcomings of traditional NDO.

C. Stability Analysis

Theorem 1: Considering PMSMDS dynamic model (4) satisfying *Assumptions 1 and 2*. The main controller (10), adaptive control gain (11), and RBFNNDO (18) with neural network weight adaptive law (23), are designed as $w_1 > 0$, $w_2 > 0$, $\frac{\lambda_{\min}(\Gamma_2)}{2\lambda_{\max}^{1/2}(\Gamma_1)} - \frac{1}{2\lambda_{\min}^{1/2}(\Gamma_1)} > 0$, $\lambda_{\min}(\Gamma_1) k_t \sqrt{2\eta_1} > 0$, and $\lambda_{\min}(\Gamma_1) \sqrt{2\eta_2} > 0$, the composite control confirms that

PMSMDS is FTC and all the errors will converge into a region near the origin.

Proof: Based on the abovementioned derivation, for the evaluation of the closed-loop stability of PMSMDS, this article chooses a Lyapunov function

$$V = V_0 + \frac{1}{2\delta_1}\tilde{\alpha}_1^2 + \frac{1}{2\delta_1}\tilde{\alpha}_2^2 + \frac{1}{2\eta_1}\tilde{D}^2 + \frac{1}{2\eta_2}\tilde{W}^{\mathrm{T}}\tilde{W}. \quad (25)$$

The derivative of V is given by

$$\dot{V} = \dot{V}_0 + \delta_1^{-1}\tilde{\alpha}_1\dot{\tilde{\alpha}}_1 + \delta_2^{-1}\tilde{\alpha}_2\dot{\tilde{\alpha}}_2 + \eta_1^{-1}\tilde{D}\dot{\tilde{D}} + \eta_2^{-1}\tilde{W}^{\mathrm{T}}\dot{\tilde{W}}. \quad (26)$$

Substituting (17) into (26), and then the derivative of V can be obtained as

$$\begin{aligned}\dot{V} \leq & -\frac{\lambda_{\min}(\Gamma_2)}{2\lambda_{\max}^{1/2}(\Gamma_1)}\left(\Phi^{\mathrm{T}}\Gamma_1\Phi\right)^{1/2} - \frac{w_1}{\sqrt{2\delta_1}}|\tilde{\alpha}_1| - \frac{w_2}{\sqrt{2\delta_2}}|\tilde{\alpha}_2| \\ & - \lambda_{\min}(\Gamma_1)k_t\left|\tilde{D}\right| - \lambda_{\min}(\Gamma_1)k_t\left\|\tilde{W}^{\mathrm{T}}\right\| \\ & + \lambda_{\min}(\Gamma_1)k_t\left\|\tilde{W}^{\mathrm{T}}\right\| + \lambda_{\min}(\Gamma_1)\left|\tilde{F}(x)\right| \\ & + \eta_1^{-1}\tilde{D}\dot{\tilde{D}} + \eta_2^{-1}\tilde{W}^{\mathrm{T}}\dot{\tilde{W}} + \delta_1^{-1}\tilde{\alpha}_1\dot{\tilde{\alpha}}_1 + \delta_2^{-1}\tilde{\alpha}_2\dot{\tilde{\alpha}}_2 \\ & + \frac{w_1}{\sqrt{2\delta_1}}|\tilde{\alpha}_1| + \frac{w_2}{\sqrt{2\delta_2}}|\tilde{\alpha}_2|. \end{aligned} \quad (27)$$

Substituting (19), (23) and (24) into (27), and considering the *Assumptions 1 and 2*, the result is simplified as

$$\begin{aligned}\dot{V} \leq & -\frac{\lambda_{\min}(\Gamma_2)}{2\lambda_{\max}^{1/2}(\Gamma_1)}\left(\Phi^{\mathrm{T}}\Gamma_1\Phi\right)^{1/2} - \frac{w_1}{\sqrt{2\delta_1}}|\tilde{\alpha}_1| - \frac{w_2}{\sqrt{2\delta_2}}|\tilde{\alpha}_2| \\ & - \lambda_{\min}(\Gamma_1)k_t\left|\tilde{D}\right| - \lambda_{\min}(\Gamma_1)\left\|\tilde{W}^{\mathrm{T}}\right\| + \tau\tilde{W}^{T}\hat{W} \\ & + \lambda_{\min}(\Gamma_1)\left\|\tilde{W}^{\mathrm{T}}\right\| + \lambda_{\min}(\Gamma_1)k_t\|h(x)\|\left\|\tilde{W}^{\mathrm{T}}\right\| \\ & + \lambda_{\min}(\Gamma_1)k_t|\varepsilon_W| + |\Phi_1|^{1/2}\mathrm{sgn}(\Phi_1)\tilde{W}^{\mathrm{T}}h(x) \\ & - |\tilde{\alpha}_1|\left(\delta_1^{-1}\dot{\hat{\alpha}}_1 - \frac{w_1}{\sqrt{2\delta_1}}\right) - |\tilde{\alpha}_2|\left(\delta_2^{-1}\dot{\hat{\alpha}}_2 - \frac{w_2}{\sqrt{2\delta_2}}\right). \end{aligned} \quad (28)$$

Based on the Young's inequality and the basis function boundary, the following can be obtained:

$$\begin{cases} h^{\mathrm{T}}(x)h(x) \leq \frac{m}{\sqrt{2\pi}b} \\ \tau\tilde{W}^{\mathrm{T}}\hat{W} \leq \tau\left(-\frac{1}{2}\left\|\tilde{W}\right\|^2 + \frac{1}{2}\|W^*\|^2\right) \leq \tau\mu_{\max}^2 \\ |\Phi_1|^{1/2}\mathrm{sgn}(\Phi_1)\tilde{W}^{\mathrm{T}}h(x) \leq \frac{V_0^{1/2}}{2\lambda_{\min}^{1/2}(\Gamma_1)} + \frac{m}{2\sqrt{2\pi}b}\tilde{W}^{\mathrm{T}}\tilde{W}. \end{cases} \quad (29)$$

Therefore, (28) can be transformed as follows:

$$\begin{aligned}\dot{V} \leq & -\left(\frac{\lambda_{\min}(\Gamma_2)}{2\lambda_{\max}^{1/2}(\Gamma_1)} - \frac{1}{2\lambda_{\min}^{1/2}(\Gamma_1)}\right)\left(\Phi^{\mathrm{T}}\Gamma_1\Phi\right)^{1/2} \\ & - \frac{w_1}{\sqrt{2\delta_1}}|\tilde{\alpha}_1| - \frac{w_2}{\sqrt{2\delta_2}}|\tilde{\alpha}_2| - \lambda_{\min}(\Gamma_1)k_t\left|\tilde{D}\right| \\ & - \lambda_{\min}(\Gamma_1)\left\|\tilde{W}^{\mathrm{T}}\right\| + \frac{\lambda_{\min}^2(\Gamma_1)}{2} + \frac{(\lambda_{\min}(\Gamma_1)k_t)^2}{2} \\ & + \left(\frac{m}{\sqrt{2\pi}b} + \frac{1}{2} - \frac{\tau}{2}\right)\tilde{W}^{\mathrm{T}}\tilde{W} + \lambda_{\min}(\Gamma_1)k_t\varepsilon_{W\max} \\ & + \tau\mu_{\max}^2 - |\tilde{\alpha}_1|\left(\delta_1^{-1}\dot{\hat{\alpha}}_1 - \frac{w_1}{\sqrt{2\delta_1}}\right) - |\tilde{\alpha}_2|\left(\delta_2^{-1}\dot{\hat{\alpha}}_2 - \frac{w_2}{\sqrt{2\delta_2}}\right). \end{aligned} \quad (30)$$

1) *Case 1:* Here, when $s > \ell$, substitute (11) into (30) and design ε and τ as $\varepsilon = \frac{w_2\sqrt{2\delta_2}}{2w_1\sqrt{2\delta_1}}$ and $\tau = 1 + \frac{2m}{\sqrt{2\pi}b}$. According to the inequality $\sqrt{a^2 + b^2 + c^2} \leq |a| + |b| + |c|$, (30) can be expressed as

$$\begin{aligned}\dot{V} \leq & -\left(\frac{\lambda_{\min}(\Gamma_2)}{2\lambda_{\max}^{1/2}(\Gamma_1)} - \frac{1}{2\lambda_{\min}^{1/2}(\Gamma_1)}\right)\left(\Phi^{\mathrm{T}}\Gamma_1\Phi\right)^{1/2} \\ & - \frac{w_1}{\sqrt{2\delta_1}}|\tilde{\alpha}_1| - \frac{w_2}{\sqrt{2\delta_2}}|\tilde{\alpha}_2| - \lambda_{\min}(\Gamma_1)k_t\left|\tilde{D}\right| \\ & - \lambda_{\min}(\Gamma_1)\left\|\tilde{W}^{\mathrm{T}}\right\| + \frac{\lambda_{\min}^2(\Gamma_1)}{2} + \frac{(\lambda_{\min}(\Gamma_1)k_t)^2}{2} \\ & + \lambda_{\min}(\Gamma_1)k_t\varepsilon_{W\max} + \tau\mu_{\max}^2 \\ \leq & -\xi_1V^{1/2} + \Xi_1 \end{aligned} \quad (31)$$

$$\text{where}\begin{cases} \xi_1 = \min\left\{\begin{matrix}\frac{\lambda_{\min}(\Gamma_2)}{2\lambda_{\max}^{1/2}(\Gamma_1)} - \frac{1}{2\lambda_{\min}^{1/2}(\Gamma_1)}, w_1, w_2, \\ \lambda_{\min}(\Gamma_1)k_t\sqrt{2\eta_1}, \lambda_{\min}(\Gamma_1)\sqrt{2\eta_2}\end{matrix}\right\} \\ \Xi_1 = \lambda_{\min}^2(\Gamma_1)/2 + (\lambda_{\min}(\Gamma_1)k_t)^2/2 \\ \qquad + \lambda_{\min}(\Gamma_1)k_t\varepsilon_{W\max} + \tau\mu_{\max}^2. \end{cases}$$

2) *Case 2:* When $s < -\ell$, substitute (11) into (30), and it can be expressed as

$$\begin{aligned}\dot{V} \leq & -\left(\frac{\lambda_{\min}(\Gamma_2)}{2\lambda_{\max}^{1/2}(\Gamma_1)} - \frac{1}{2\lambda_{\min}^{1/2}(\Gamma_1)}\right)\left(\Phi^{\mathrm{T}}\Gamma_1\Phi\right)^{1/2} \\ & - \frac{w_1}{\sqrt{2\delta_1}}|\tilde{\alpha}_1| - \frac{w_2}{\sqrt{2\delta_2}}|\tilde{\alpha}_2| - \lambda_{\min}(\Gamma_1)k_t\left|\tilde{D}\right| \\ & - \lambda_{\min}(\Gamma_1)\left\|\tilde{W}^{\mathrm{T}}\right\| + \frac{\lambda_{\min}^2(\Gamma_1)}{2} + \frac{(\lambda_{\min}(\Gamma_1)k_t)^2}{2} \\ & + \lambda_{\min}(\Gamma_1)k_t\varepsilon_{W\max} + \tau\mu_{\max}^2 + |\tilde{\alpha}_1|\frac{2w_1}{\sqrt{2\delta_1}} \\ & + |\tilde{\alpha}_2|\left(2\delta_2^{-1}\varepsilon w_1\sqrt{\frac{\delta_1}{2}} + \frac{w_2}{\sqrt{2\delta_2}}\right) \\ \leq & -\xi_2V^{1/2} + \Xi_2 \end{aligned} \quad (32)$$

$$\text{where}\begin{cases} \xi_2 = \min\left\{\begin{matrix}\frac{\lambda_{\min}(\Gamma_2)}{2\lambda_{\max}^{1/2}(\Gamma_1)} - \frac{1}{2\lambda_{\min}^{1/2}(\Gamma_1)}, w_1, w_2, \\ \lambda_{\min}(\Gamma_1)k_t\sqrt{2\eta_1}, \lambda_{\min}(\Gamma_1)\sqrt{2\eta_2}\end{matrix}\right\} \\ \Xi_2 = \lambda_{\min}^2(\Gamma_1)/2 + (\lambda_{\min}(\Gamma_1)k_t)^2/2 + \tau\mu_{\max}^2 \\ \qquad + \lambda_{\min}(\Gamma_1)k_t\varepsilon_{W\max} + |\tilde{\alpha}_1|\frac{2w_1}{\sqrt{2\delta_1}} \\ \qquad + |\tilde{\alpha}_2|(2\delta_2^{-1}\varepsilon w_1\sqrt{\frac{\delta_1}{2}} + \frac{w_2}{\sqrt{2\delta_2}}). \end{cases}$$

3) *Case 3:* Similarly, when $|s| \leq \ell$, $\dot{\hat{\alpha}}_1 = 0$, one can obtain

$$\begin{cases} \xi_3 = \xi_2 = \min\left\{\begin{matrix}\frac{\lambda_{\min}(\Gamma_2)}{2\lambda_{\max}^{1/2}(\Gamma_1)} - \frac{1}{2\lambda_{\min}^{1/2}(\Gamma_1)}, w_1, w_2, \\ \lambda_{\min}(\Gamma_1)k_t\sqrt{2\eta_1}, \lambda_{\min}(\Gamma_1)\sqrt{2\eta_2}\end{matrix}\right\} \\ \Xi_3 = \lambda_{\min}^2(\Gamma_1)/2 + (\lambda_{\min}(\Gamma_1)k_t)^2/2 + \tau\mu_{\max}^2 \\ \qquad + \lambda_{\min}(\Gamma_1)k_t\varepsilon_{W\max} + \frac{w_1}{\sqrt{2\delta_1}}|\tilde{\alpha}_1| + \frac{w_2}{\sqrt{2\delta_2}}|\tilde{\alpha}_2|. \end{cases} \quad (33)$$

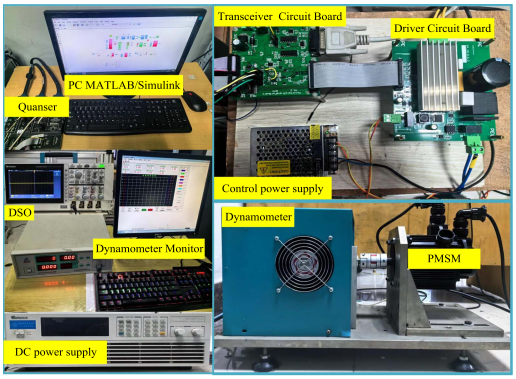

Fig. 4. PMSMDS drive test setup.

TABLE I
PARAMETERS IN THE PMSMDS

Parameter	Value	Parameter	Value
Rated power	0.95 kW	d-axis inductance (L_d)	2.5 mH
Rated speed	1.5 krpm	q-axis inductance (L_q)	3.1 mH
Rated current	4.3 A	Stator resistance (R_s)	1.35 Ω
Rated voltage	220 V	Magnetic flux (ϕ_f)	0.1552 V.s
Pole pairs (n_p)	4	Moment of inertia (J)	1.26 g.m^2

TABLE II
PARAMETERS OF DIFFERENT CONTROLLERS

Controllers	Parameters
PI	$k_p = 0.15$, $k_i = 2.2$
ISMC	G = [70 1 0], β = 1200, γ = 300
Composite controller	G = [500 1], $c_j = \begin{bmatrix} -10 & -5 & 0 & 5 & 10 \\ -50 & -25 & 0 & 25 & 50 \end{bmatrix}$ b = [200 200 200 200 200], η_2 = 10, τ = 1.28 ω_1 = 1500, δ_1 = 0.5, ℓ = 5, ε = 6, η_1 = 0.01
Current controller	k_{qp}=2.5, k_{qi}=1200, k_{dp}=2.2, k_{di}=1200

Remark 7: Based on (31)–(33) and FTC stability principle [31], following the parameter design rule in *Theorem 1*, the abovementioned analysis demonstrates that all closed-loop signals are bounded, and the tracking error converges to a neighborhood of the origin within a fixed time.

IV. EXPERIMENTAL RESULTS

In order to verify the effectiveness and practicality of the proposed composite controller, a PMSMDS drive test setup is built as illustrated in Fig. 4. The test setup consists of a Quanser system, a driver circuit board, a transceiver circuit board, a dynamometer, and a PMSM. The PMSM parameters are listed in Table I. The sampling frequencies of the speed and current loops are chosen as 1 kHz and 10 kHz, respectively. The control algorithms are executed in the Quanser system. The comparison studies with PI, integral SMC (ISMC), AIHOSMC, AIHOSMC+NDO, and AIHOSMC+RBFNNDO (the composite controller) are implemented from three aspects of tracking performance, antidisturbance capability, and robustness. The controller parameters are shown in Table II.

Remark 8: The following gives the selection method of the controller parameters in details.

For ISMC, g+p satisfies Hurwitz, and p is a Laplace operator, a larger g may lead to significant overshoot, and the selection of g involves a trial-and-error process with g <1000. β and γ are necessary conditions to ensure that the tracking error approaches zero after the system state reaches the sliding surface. In theory, the larger γ, the faster the system convergence speed, the greater the overshoot, and the larger β, the greater the system tracking error.

For AIHOSMC, as adaptive gains, larger positive real numbers δ_1, w_1, ε and will result in smaller tracking errors and faster convergence speeds. The parameters based on the FTC stability principle should simultaneously satisfy $\varepsilon = w_2\sqrt{2\delta_2}/2w_1\sqrt{2\delta_1}$.

For NDO, $\eta_1 > 0$ is the observer gain, and the larger η_1, the faster the observer convergence speed, but the observation error is also larger and overshoot may occur during the convergence process.

For RBFNN, n is related to the system state, and c_j and m should cover the entire range of input vector. Generally, the larger m, the better the approximation performance of RBFNN, but the corresponding computational cost is also higher. b_j determines the influence range or locality of each basis function, and continuously adjusts it through experiments until the most suitable width is determined to ensure optimal performance. Selecting adaptive gain $\eta_2 > 0$ and $\tau > 0$ to ensure system stability, and then further adjusting them to enhance closed-loop tracking performance, the larger τ, the faster the convergence speed of the neural network, but the oscillation around the weights will eventually become larger, indicating no absolute convergence. The parameters based on the FTC stability principle should simultaneously satisfy $\tau = 1 + 2m/\sqrt{2\pi}b$. η_2 is closely related to the adjustment time and overall stability: A larger one will adjust the control input more quickly, but it will lead to a decrease in system stability; a smaller one will cause the system to react slowly and cannot effectively correct system deviations. The selection of η_2 should ensure that the system can effectively respond to parameter changes and external disturbances, while avoiding overcompensation or instability.

For the current controller, PI is used to achieve a good balance between tracking accuracy and computational burden. In practice, the null-pole cancellation method is generally used, but fine tuning is still needed on this basis to ensure optimal system operation.

A. Low-Speed Tracking Accuracy Experiment

1) *Group-1. Tracking Performance of Suddenly Changing Speed Without Load:* The experimental results obtained from a step change of the reference speeds between 5 and 15 rpm are shown in Fig. 5. As illustrated in Fig. 5(a) and (b), when the reference speed steps from 5 to 15 r/min, PMSMDS using PI and ISMC reach the reference speed in about 0.43 s and 0.46 s, respectively, with overshoots of 9.35 r/min and 10.18 r/min, respectively. The stabilization times for AIHOSMC and AIHOSMC+NDO are 0.58 s

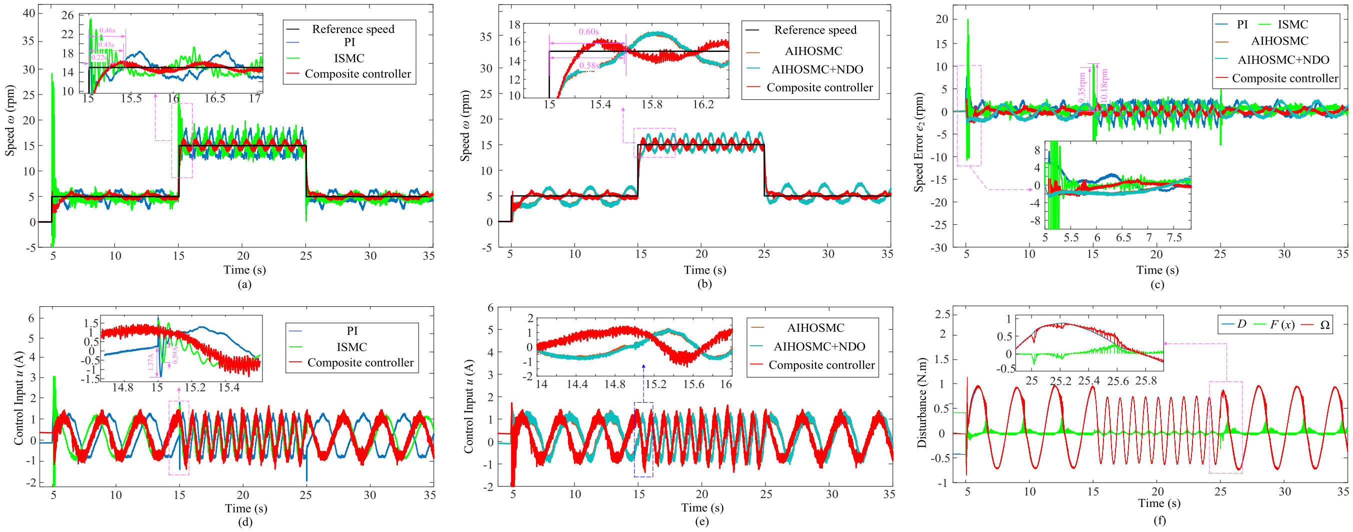

(a)

(b)

(c)

(d)

(e)

(f)

Fig. 5. Tracking performance of suddenly changing speed without load for different controllers. (a) and (b) Speed responses. (c) Speed error responses. (d) and (e) Control input responses. (f) Estimated values of disturbances.

and 0.6 s, respectively. In contrast, the system with the composite controller exhibits a shorter stabilization time of around 0.22 s and shows no significant overshoot. As seen in Fig. 5(c), the start-up performances of PI and ISMC are suboptimal, with noticeable vibrations, whereas composite controller achieves a smooth start. At the steady-state speeds of 5 r/min and 15 r/min, the maximum absolute values of tracking errors for PI, ISMC, AIHOSMC, AIHOSMC+NDO, and composite controller are 2.47 r/min and 3.34 r/min, 2.71 r/min and 4.46 r/min, 2.11 r/min and 2.05 r/min, 2.12 r/min and 2.04 r/min, and 0.91 r/min and 1.23 r/min, respectively. Adaptive control gains can significantly reduce tracking errors and chatters. As shown in Fig. 5(d) and (e), during a sudden change in speed, there is a drop in the control input signals for PI and ISMC (-1.37 A and -0.59 A, respectively). However, the compensation effect of composite controller prevents any drop in the control input signal. Fig. 5(f) demonstrates that RBFNNDO effectively observes the fast-changing disturbances present in the system at all times and compensates for them in the control input, thereby reducing steady-state errors and improve the robustness of the system during transients.

2) *Group-2. Tracking Performance of Continuously Changing Speed Without Load:* To evaluate the performance of the composite controller under continuously changing speed, the reference speed signal is configured as both a step signal at 10 r/min and a sine signal given by $5\sin(0.4\pi t)$ r/min. The experimental results are shown in Fig. 6. As shown in Fig. 6(a) and (b), when reference is a sine signal, the maximum absolute values of tracking errors for PI, ISMC, AIHOSMC, AIHOSMC+NDO, and composite controller are 3.47 r/min, 3.38 r/min, 2.11 r/min, 1.94 r/min, and 1.01 r/min, respectively.

In Fig. 6(d), compared to a constant speed, when the speed changes sinusoidally, the value of the fast-changing disturbance will increase and change more irregularly. However, due to the addition of RBFNNDO, the system can effectively compensate for this part of the disturbance [see Fig. 6(c)] and improve tracking performance of the system. It is obvious that the control effect of composite controller is better than that of the other four controllers, and it has better adaptability to constantly changing speed. Detailed performance comparison results of tracking accuracy are shown in Table III.

TABLE III
DETAILED PERFORMANCE RESULTS OF TRACKING ACCURACY

Controllers	Setting time (s)	Transient Maximum Speed (rpm)	Steady-state Error (rpm)		
			Group-1		*Group-2*
PI	0.43	24.35	2.47	3.34	3.47
ISMC	0.46	25.18	2.71	4.46	3.38
AIHOSMC	0.58	17.18	2.11	2.05	2.11
AIHOSMC+NDO	0.60	17.18	2.12	2.04	1.94
Composite controller	0.22	16.02	0.91	1.23	1.01

B. Antidisturbance Experiment

In this section, the speed fluctuations caused by load torque disturbances are evaluated. In the first test, the reference speed remains unchanged at 10 r/min, and a load torque of 0.5 N · m is applied at $t = 15$ s and removed $t = 25$ s, respectively. Fig. 7 depicts the experimental results of the speed and q-axis current. It can be clearly seen from Fig. 7(a) that the speeds drop with load torque under the control of PI, AIHOSMC, AIHOSMC+NDO, and the composite controller are 4.92 r/min, 6.98 r/min, 8.33 r/min, and 8.99 r/min, respectively. When the 0.5 N · m load is suddenly added at $t = 15$ s, composite controller exhibits the most excellent characteristics.

Due to the limited antidisturbance capabilities of PI and AIHOSMC, their speeds drop significantly after the load is increased, making speeds recovery difficult. As shown in Fig. 7(b) and (c), the presence of NDO enables both the AIHOSMC+NDO and composite controller to resist slow-changing load torque.

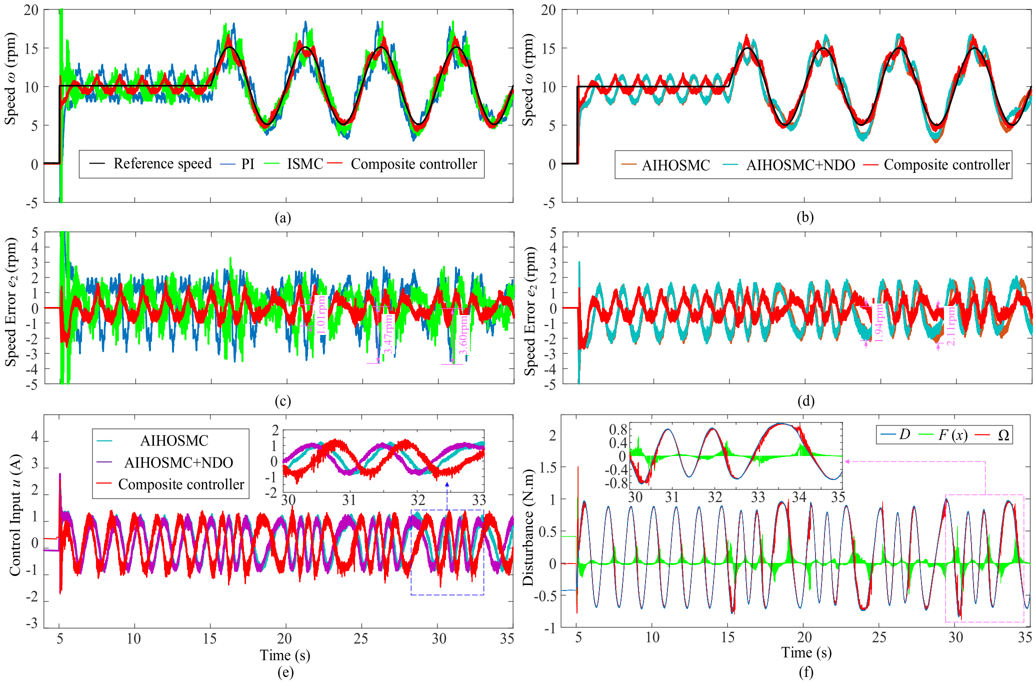

Fig. 6. Tracking performance of continuously changing speed without load for different controllers. (a) and (b) Speed responses. (c) and (d) Speed error responses. (e) Control input responses. (f) Estimated values of disturbances.

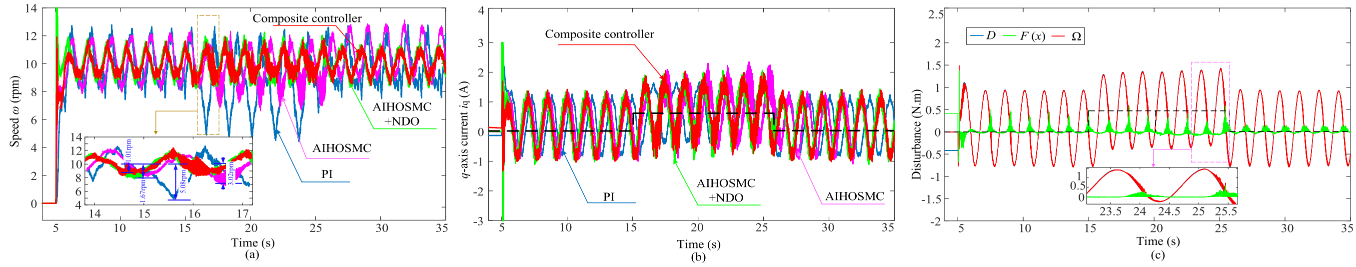

Fig. 7. Tracking performance of constant speed with load step up for different controllers. (a) Speed responses. (b) q-axis current responses. (c) Estimated values of disturbances.

TABLE IV
DETAILED PERFORMANCE RESULTS WITH LOAD STEP UP

Controllers	Recovery Time (s)	Speed Drop (rpm)
PI	1.96	5.08
AIHOSMC	2.04	3.02
AIHOSMC+NDO	1.22	1.67
Composite controller	1.15	1.01

After the load is applied, there is no significant speed drop compared to the no-load condition. For fast-changing disturbances, RBFNNDO exhibits significant real-time adaptive training capability, effectively attenuating relevant load disturbances and enhancing the robustness of the system. Consequently, using composite controller minimizes the impact of disturbances on the system and exhibits the smallest steady-state error. Detailed performance results with load step up are shown in Table IV.

In addition, harmonic suppression controller (HSC) is an advanced speed control strategy [33], [34]. To verify whether HSC is suitable for PMSMDS low-speed control, further analysis of performance is conducted for PI, PI+HSC (in [33]), and composite controller. The experimental results are shown in Fig. 8. It can be seen that after applying a load of 0.5 $\mathrm{N \cdot m}$ to the system, the maximum absolute values of tracking errors for PI, PI+HSCS, and composite controller are 8.23 r/min, 6.11 r/min, and 2.18 r/min, respectively. Compared with PI, PI+HSCS reduces speed ripple and improves low-speed performance. It suppresses disturbance from a distinctive perspective, improves current smoothness and overall performance. The ripple of composite controller is minimal. After compensating for the fast-changing and slow-changing disturbance, it improves the overall smoothness of the q-axis and A-phase current. Compared with other controllers, the improvement effect is the most obvious. The current analysis results in Fig. 8 also demonstrate the strength of composite controller in minimizing current ripple.

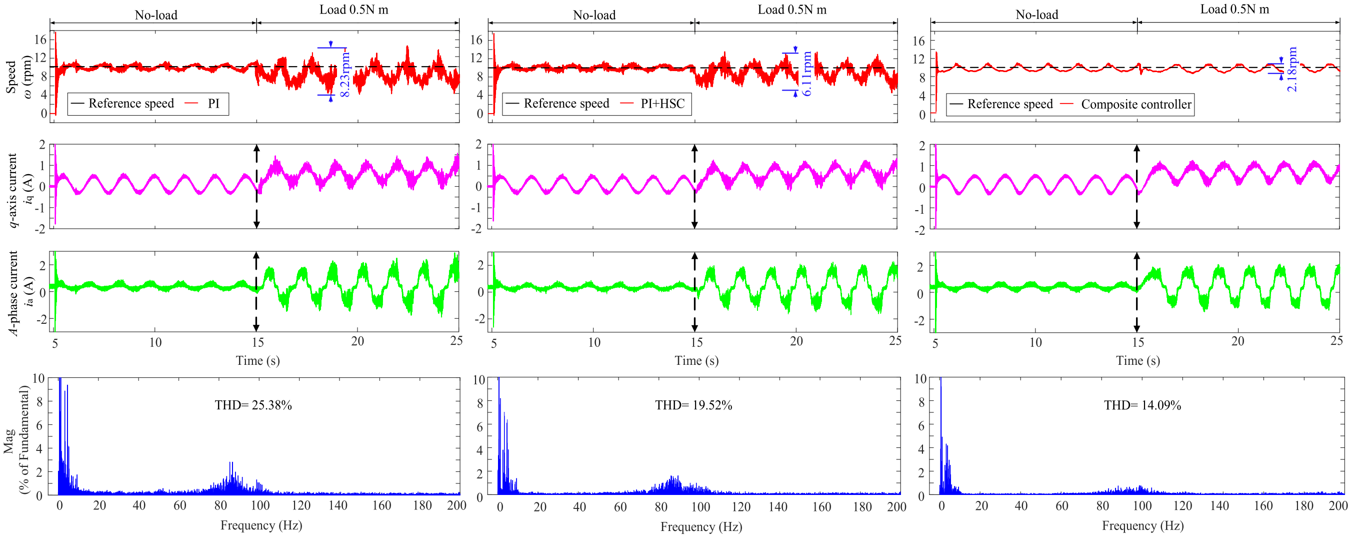

(a) (b) (c)

Fig. 8. Experimental results of current and harmonic for different controllers (a) PI. (b) PI+HSCS. (c) Proposed composite controller.

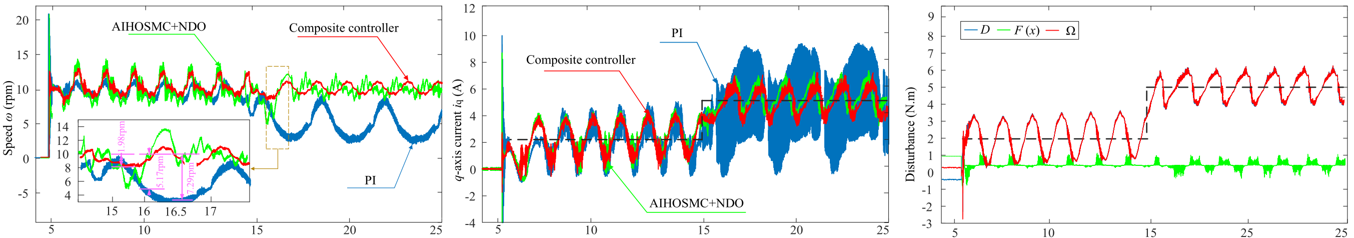

(a) (b) (c)

Fig. 9. Tracking performance of constant speed with rated load for different controllers. (a) Speed responses. (b) q-axis current responses. (c) Estimated values of disturbances.

TABLE V
DETAILED PERFORMANCE RESULTS WITH RATED LOAD

Controllers	Recovery Time (s)	Speed Drop (rpm)
PI	1.98	7.29
AIHOSMC+NDO	1.45	5.17
Composite controller	1.04	1.98

The total harmonic distortion of PI is 25.38%, PI+HSCS is 19.52%, and composite controller is 14.09%.

In the second test, the speed and q-axis current responses are evaluated under rated load torque. The reference speed is also set to 10 r/min. Fig. 9 and Table V show the detailed experimental results. As shown in Fig. 9(a), composite controller achieves the best transient speed tracking and steady-state performance at 2 N · m load start-up. Furthermore, when the load torque changes to the rated load torque of 5 N.m at $t = 15$ s, composite controller maintains nearly no significant speed drop, achieving the optimal speed tracking curve within 0.5 s. In contrast, the speed drops for the PI and AIHOSMC+NDO are 7.29 r/min and 5.17 r/min, respectively, with PI demonstrating the worst robustness. As shown in Fig. 9(b), the q-axis current response of composite controller also provides an excellent performance, exhibiting minimal ripple and smoothness at 2 N · m start-up and 5 N · m rated load. The current ripple of PI is the largest, and its ability to cope with rated torque is insufficient, while NDO can effectively compensate. As shown in Fig. 9(c), the disturbance estimation results clearly indicate that the good tracking performance and antidisturbance capabilities of composite controller are due to the accurate approximation and compensation of the RBFNN for fast-changing disturbances. The proposed composite controller has the strongest robustness under variable load conditions.

C. Parameter Uncertainty Robustness Experiment

The motor parameters in (4) are difficult to accurately determine due to influences from both the motor itself and external operating conditions. This means that the motor parameters used in the controller may differ from the actual motor parameters. Therefore, experiments are conducted by increasing and decreasing the moment of inertia J in the motor model within the controller by 20% in (5) to more effectively verify the performance of the composite controller.

The speed tracking performance under parameter uncertainty is shown in Fig. 10(a). It can be observed that, under parameter variations, the speed tracking error of AIHOSMC is larger

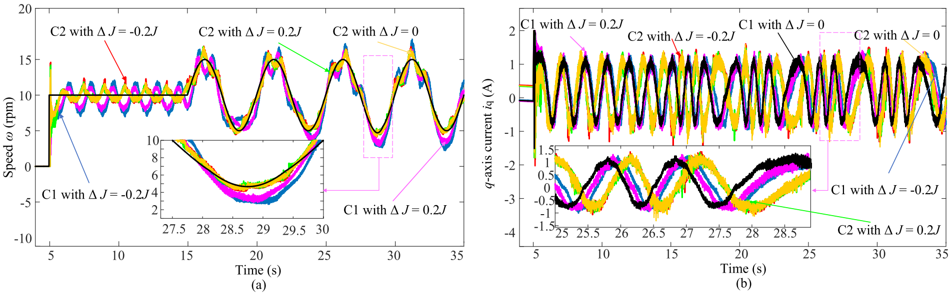

Fig. 10. Tracking performance with parameter uncertainty for AIHOSMC (C1) and the composite controller (C2). (a) Speed responses. (b) q-axis current responses.

TABLE VI
DETAILED PERFORMANCE RESULTS WITH PARAMETER VARIATIONS

Speed Vars. Para. Vars. Controllers	ΔJ=0.2J	ΔJ=0J	ΔJ=-0.2J
AIHOSMC	1.78	2.11	2.32
Composite contoller	0.26	0.25	0.28

than that of composite controller, and the error of AIHOSMC tends to increase over time. This suggests that if the system continues to run, its tracking performance will degrade, whereas the control performance of composite controller remains largely unaffected by parameter changes. Detailed performance results with parameter variations are shown in Table VI.

The q-axis current is shown in Fig. 10(b). When AIHOSMC is used under parameter variations, the control input fluctuates significantly and is highly sensitive to complex operating conditions. In contrast, composite controller shows strong resilience to parameter changes, with its control input remaining almost unchanged during these variations. This indicates that composite controller maintains superior control performance for PMSMDS under complex operating conditions.

V. CONCLUSION

This article proposes an adaptive integral high-order sliding-mode low-speed controller based on RBFNNDO, aimed to improve low-speed tracking accuracy and antidisturbance capability. Comparative experiments are conducted on PI, ISMC, AIHOSMC, AIHOSMC+NDO, and the proposed composite controller. The experimental results showed that composite controller outperformed the other four controllers in terms of low-speed tracking error, convergence speed, antidisturbance capability, and robustness. Adaptive control gains can achieve FTC of the system, and RBFNNDO can effectively observe both the fast-changing and slow-changing disturbances of PMSMDS. The proposed composite controller has enhanced robustness and superior dynamic performance.

REFERENCES

[1] M. Ghods, J. Faiz, M. A. Bazrafshan, H. Gorginpour, and M. S. Toulabi, "Design of an L-shaped array Vernier permanent magnet machine for unmanned aerial vehicle propulsion using a Schwarz–Christoffel mapping-based equivalent magnetic network model," *IEEE Trans. Ind. Electron.*, vol. 71, no. 1, pp. 237–249, Jan. 2024.

[2] A. Allca-Pekarovic, P. J. Kollmeyer, A. Forsyth, and A. Emadi, "Experimental characterization and modeling of a YASA P400 axial flux PM traction machine for performance analysis of a chevy bolt EV," *IEEE Trans. Ind. Appl.*, vol. 60, no. 2, pp. 3108–3119, Mar./Apr. 2024.

[3] W. L. Yin, X. Wu, and X. M. Rui, "Adaptive robust backstepping control of the speed regulating differential mechanism for wind turbines," *IEEE Trans. Sustain. Energy*, vol. 10, no. 3, pp. 1311–1318, Jul. 2019.

[4] H. T. Li, S. Y. Yang, and Y. Le, "Torque ripple minimization of low-speed gimbal servo system using parameter-optimized ESO," *IEEE J. Emerg. Sel. Topics Power Electron.*, vol. 11, no. 2, pp. 2094–2103, Apr. 2023.

[5] Q. Ni et al., "A new position and speed estimation scheme for position control of PMSM drives using low-resolution position sensors," *IEEE Trans. Ind. Appl.*, vol. 55, no. 4, pp. 3747–3758, Jul./Aug. 2019.

[6] C. Wang, J. D. Peng, and J. F. Pan, "A novel friction compensation method based on stribeck model with fuzzy filter for PMSM servo systems," *IEEE Trans. Ind. Electron.*, vol. 70, no. 12, pp. 12124–12133, Dec. 2023.

[7] C. B. Yang, B. Song, Y. L. Xie, S. Q. Zheng, and X. Q. Tang, "Adaptive identification of nonlinear friction and load torque for PMSM drives via a parallel-observer-based network with model compensation," *IEEE Trans. Power Electron.*, vol. 38, no. 5, pp. 5875–5897, May 2023.

[8] S. B. Wang and J. Na, "Parameter estimation and adaptive control for servo mechanisms with friction compensation," *IEEE Trans. Ind. Informat.*, vol. 16, no. 11, pp. 6816–6825, Nov. 2020.

[9] H. Q. Chu, B. Z. Gao, W. L. Gu, and H. Chen, "Low-speed control for permanent-magnet DC torque motor using observer-based nonlinear triple-step controller," *IEEE Trans. Ind. Electron.*, vol. 64, no. 4, pp. 3286–3296, Apr. 2017.

[10] B. Ding, D. Xu, B. Jiang, P. Shi, and W. Yang, "Disturbance-observer-based terminal sliding mode control for linear traction system with prescribed performance," *IEEE Trans. Transp. Electrific.*, vol. 7, no. 2, pp. 649–658, Jun. 2021.

[11] A. Apte, V. A. Joshi, H. Mehta, and R. Walambe, "Disturbance-observer-based sensorless control of PMSM using integral state feedback controller," *IEEE Trans. Power Electron.*, vol. 35, no. 6, pp. 6082–6090, Jun. 2020.

[12] Z. Xu, T. Zhang, Y. Bao, H. Zhang, and C. Gerada, "A nonlinear extended state observer for rotor position and speed estimation for sensorless IPMSM drives," *IEEE Trans. Power Electron.*, vol. 35, no. 1, pp. 733–743, Jan. 2020.

[13] J. Han, "From PID to active disturbance rejection control," *IEEE Trans. Ind. Electron.*, vol. 56, no. 3, pp. 900–906, Mar. 2009.

[14] C. Hua, "Disturbance observer based control for nonlinear systems," *IEEE/ASME Trans. Mechatron.*, vol. 9, no. 4, pp. 706–710, Dec. 2004.

[15] Z. J. Hao et al., "Linear/nonlinear active disturbance rejection switching control for permanent magnet synchronous motors," *IEEE Trans. Power Electron.*, vol. 36, no. 8, pp. 9334–9347, Aug. 2021.

[16] C. Y. Pan, Z. X. Peng, S. C. Yang, G. G. Wen, and T. W. Huang, "Adaptive neural network-based prescribed-time observer for battery state-of-charge estimation," *IEEE Trans. Power Electron.*, vol. 38, no. 1, pp. 165–176, Jan. 2023.

[17] M. Chen and S. S. Ge, "Adaptive neural output feedback control of uncertain nonlinear systems with unknown hysteresis using disturbance observer," *IEEE Trans. Ind. Electron.*, vol. 62, no. 12, pp. 7706–7716, Dec. 2015.

[18] R. C. Li, Y. Yang, and Q. L. Zhang, "Neural network based adaptive SMO design for T-S fuzzy descriptor systems," *IEEE Trans. Fuzzy Syst.*, vol. 28, no. 10, pp. 2605–2618, Oct. 2020.

[19] J. W. Ma, H. Q. Wang, and J. F. Qiao, “Adaptive neural fixed-time tracking control for high-order nonlinear systems,” *IEEE Trans. Neural Netw. Learn. Syst.*, vol. 35, no. 1, pp. 708–717, Jan. 2024.

[20] F. F. M. El-Sousy, M. M. Amin, and O. A. Mohammed, “Robust adaptive neural network tracking control with optimized super-twisting sliding-mode technique for induction motor drive system,” *IEEE Trans. Ind. Appl.*, vol. 58, no. 3, pp. 4134–4157, May/Jun. 2022.

[21] X. P. Lin et al., “Observer-based prescribed performance speed control for PMSMs: A data-driven RBF neural network approach,” *IEEE Trans. Ind. Inform.*, vol. 20, no. 5, pp. 7502–7512, May 2024.

[22] E. Chemali, P. J. Kollmeyer, M. Preindl, R. Ahmed, and A. Emadi, “Long short-term memory networks for accurate state-of-charge estimation of Li-ion batteries,” *IEEE Trans. Ind. Electron.*, vol. 65, no. 8, pp. 6730–6739, Aug. 2018.

[23] Y. F. Yin et al., “Observer-based adaptive sliding mode control of NPC converters: An RBF neural network approach,” *IEEE Trans. Power Electron.*, vol. 34, no. 4, pp. 3831–3841, Apr. 2019.

[24] H. H. Choi, H. M. Yun, and Y. Kim, “Implementation of evolutionary fuzzy PID speed controller for PM synchronous motor,” *IEEE Trans. Ind. Inform.*, vol. 11, no. 2, pp. 540–547, Apr. 2015.

[25] H. Z. Wang, S. Xu, and H. S. Hu, “PID controller for PMSM speed control based on improved quantum genetic algorithm optimization,” *IEEE Access*, vol. 11, pp. 61091–61102, 2023.

[26] C. J. Lin, H. T. Yau, and Y. C. Tian, “Identification and compensation of nonlinear friction characteristics and precision control for a linear motor stage,” *IEEE/ASME Trans. Mechatron.*, vol. 18, no. 4, pp. 1385–1396, Aug. 2013.

[27] W. Xu, A. K. Junejo, Y. Liu, M. G. Hussien, and J. Zhu, “An efficient antidisturbance sliding-mode speed control method for PMSM drive systems,” *IEEE Trans. Power Electron.*, vol. 36, no. 6, pp. 6879–6891, Jun. 2021.

[28] X. D. Sun, J. H. Cao, G. Lei, Y. G. Guo, and J. G. Zhu, “A composite sliding mode control for SPMSM drives based on a new hybrid reaching law with disturbance compensation,” *IEEE Trans. Transp. Electrific.*, vol. 7, no. 3, pp. 1427–1436, Sep. 2021.

[29] J. Yang, J. Su, S. Li, and X. Yu, “High-order mismatched disturbance compensation for motion control systems via a continuous dynamic sliding-mode approach,” *IEEE Trans. Ind. Informat.*, vol. 10, no. 1, pp. 604–614, Feb. 2014.

[30] P. Li, X. Yu, and B. Xiao, “Adaptive quasi-optimal higher order sliding-mode control without gain overestimation,” *IEEE Trans. Ind. Informat.*, vol. 14, no. 9, pp. 3881–3891, Sep. 2018.

[31] A. Saim, H. Wang, and Y. Tian, “Adaptive high-order terminal sliding mode control based on time delay estimation for the robotic manipulators with backlash hysteresis,” *IEEE Trans. Syst. Man Cybern.: Syst.*, vol. 51, no. 2, pp. 1128–1137, Feb. 2021.

[32] Y. Shtessel, M. Taleb, and F. Plestan, “A novel adaptive-gain supertwisting sliding mode controller: Methodology and application,” *Automatica*, vol. 48, no. 5, pp. 759–769, 2012.

[33] G. Feng, C. Lai, J. Tian, and N. C. Kar, “Multiple reference frame based torque ripple minimization for PMSM drive under both steady-state and transient conditions,” *IEEE Trans. Power Electron.*, vol. 34, no. 7, pp. 6685–6696, Jul. 2019.

[34] Z. Wu, Z. Yang, K. Ding, and G. He, “Order-domain-based harmonic injection method for multiple speed harmonics suppression of PMSM,” *IEEE Trans. Power Electron.*, vol. 36, no. 4, pp. 4478–4487, Apr. 2021.

Weichao Wang was born in Binzhou, China. He received the B.S. and M.S. degrees in electrical engineering from Qufu Normal University, Rizhao, China, in 2019 and 2021, respectively. He is currently working toward the Ph.D. degree in control science and engineering with the Nanjing University of Aeronautics and Astronautics, Nanjing, China.

His current research interests include motor drive system and its high-performance intelligent control.

Yongqiang Ye (Senior Member, IEEE) was born in Tongxiang, China. He received the B.E. and M.E. degrees from Zhejiang University, Hangzhou, China, in 1994 and 1997, respectively, and the Ph.D. degree from Nanyang Technological University, Singapore, in 2004, all in electrical engineering.

Since 2009, he has been a Professor with the College of Automation Engineering, Nanjing University of Aeronautics and Astronautics, Nanjing, China. He has authored and coauthored two books and more than 85 journal articles. His current research interests include advanced control of power electronics and electrical machines.

Xudong Chen was born in Tianjin, China. He received the B.S. degree in detection, guidance, and control technology in 2023 from the Nanjing University of Aeronautics and Astronautics, Nanjing, China, where he is currently working toward the M.S. degree in control science and engineering.

His current research interest is motor control.

Yongchao Yuan was born in Heze, China. He received the Ph.D. degree in engineering from the China Academy of Machinery Science and Technology, Beijing, China, in 2019.

Since 2020, he has been a Senior Engineer specializing in Mechanical Design and Theory. He has authored or coauthored 19 papers and obtained 24 patents, including 12 invention patents. He is currently affiliated with the China Academy of Machinery Science and Technology Qingdao Branch Company, LTD., Qingdao, China, where he is currently an Assistant to the General Manager and concurrently leads the High-End Power Equipment Business Department. His current research interest is gear mechanical transmission.